

Article

An Image-Based Framework for the Analysis of the Murine Microvasculature: From Tissue Clarification to Computational Hemodynamics

Santiago Mañosas ¹, Aritz Sanz ¹, Cristina Ederra ², Ainhoa Urbiola ², Elvira Rojas-de-Miguel ^{1,3,4}, Ainhoa Ostiz ^{1,3,4}, Iván Cortés-Domínguez ^{2,3}, Natalia Ramírez ^{1,3,4}, Carlos Ortiz-de-Solórzano ^{2,3,5}, Arantxa Villanueva ^{1,3} and Mauro Malvè ^{1,6,*}

- ¹ Department of Engineering, Campus Arrosadía s/n, Universidad Pública de Navarra (UPNA), 31006 Pamplona, Spain
 - ² Imaging Platform, Center for Applied Medical Research (CIMA), University of Navarra, 31008 Pamplona, Spain
 - ³ Instituto de Investigación Sanitaria de Navarra (IdiSNA), Irunlarrea 3, 31008 Pamplona, Spain
 - ⁴ Oncohematology Research Group, Navarrabiomed, Hospital Universitario de Navarra (HUN), Irunlarrea 3, 31008 Pamplona, Spain
 - ⁵ CIBERONC, Centro de Investigación Biomédica en Red-Cáncer, Instituto de Salud Carlos III, C/Monforte de Lemos 3-5, Pabellón 11, Planta 0, 28029 Madrid, Spain
 - ⁶ CIBER-BBN, Centro de Investigación Biomédica en Red-Bioingeniería, Biomateriales y Nanomedicina, C/Poeta Mariano Esquillor s/n, 50018 Zaragoza, Spain
- * Correspondence: mauro.malve@unavarra.es



Citation: Mañosas, S.; Sanz, A.; Ederra, C.; Urbiola, A.; Rojas-de-Miguel, E.; Ostiz, A.; Cortés-Domínguez, I.; Ramírez, N.; Ortiz-de-Solórzano, C.; Villanueva, A.; et al. An Image-Based Framework for the Analysis of the Murine Microvasculature: From Tissue Clarification to Computational Hemodynamics. *Mathematics* **2022**, *10*, 4593. <https://doi.org/10.3390/math10234593>

Academic Editor: Fernando Simoes

Received: 4 November 2022

Accepted: 28 November 2022

Published: 4 December 2022

Publisher's Note: MDPI stays neutral with regard to jurisdictional claims in published maps and institutional affiliations.

Abstract: The blood–brain barrier is a unique physiological structure acting as a filter for every molecule reaching the brain through the blood. For this reason, an effective pharmacologic treatment supplied to a patient by systemic circulation should first be capable of crossing the barrier. Standard cell cultures (or those based on microfluidic devices) and animal models have been used to study the human blood–brain barrier. Unfortunately, these tools have not yet reached a state of maturity because of the complexity of this physiological process aggravated by a high heterogeneity that is not easily recapitulated experimentally. In fact, the extensive research that has been performed and the preclinical trials carried out provided sometimes contradictory results, and the functionality of the barrier function is still not fully understood. In this study, we have combined tissue clarification, advanced microscopy and image analysis to develop a one-dimensional computational model of the microvasculature hemodynamics inside the mouse brain. This model can provide information about the flow regime, the pressure field and the wall shear stress among other fluid dynamics variables inside the barrier. Although it is a simplified model of the cerebral microvasculature, it allows a first insight on into the blood–brain barrier hemodynamics and offers several additional possibilities to systematically study the barrier microcirculatory processes.

Keywords: blood–brain barrier microvasculature; cortical capillary network; tissue clarification; imaging technique; numerical model; microvascular hemodynamics

MSC: 76-10; 92C55; 68U10; 92C10



Copyright: © 2022 by the authors. Licensee MDPI, Basel, Switzerland. This article is an open access article distributed under the terms and conditions of the Creative Commons Attribution (CC BY) license (<https://creativecommons.org/licenses/by/4.0/>).

1. Introduction

The increase of performances of the medical imaging technique in the last decades has allowed non-invasive information of geometries and associated morphologies of large cerebral arteries. In biomedical engineering, this information can be further used for generating 1D to 3D computational models to shed light on cerebrovascular hemodynamics [1,2]. Unfortunately, this process becomes more and more complicated once the vascular scale is

becoming smaller, reaching the blood–brain barrier capillaries (BBB), whose number is huge (more than 10 billion) [3].

In recent years, extensive research has been oriented toward the microcirculatory flow proposing complex mathematical models based on cerebrovascular images [3–8]. However, image segmentation has inherently several challenges. First of all, patient-specific human images are difficult to be obtained. The acquisition of the images with the necessary resolution *in vivo* is not feasible at the micro-scale. Furthermore, the use of cadavers for obtaining useful images also affects as the capillaries tend to collapse once the blood flow and pressure reduce after death [9]. For this reason, murine and rodent images have been utilized as baseline geometry for studying BBB microcirculation [10–16]. Other works have presented imaging-driven modeling for hemodynamics in zebrafish microvasculature and mammalian hearts [17–20]. Models oriented to the vascular topology and transport efficiency have been presented by Katifori and coworkers [21,22].

Nowadays, a wide range of imaging techniques are available. In the literature, corrosion casting [23], confocal microscopy [4], computerized tomography angiography and quantitative magnetic resonance angiography [2], two-photon imaging [8,24,25] and synchrotron radiation-based X-ray tomographic microscopy [26–28] have been mostly adopted depending on the specific necessities of the researchers. A combination of some of these methods can thus be of advantage for limiting the weakness of each method and it is applied in the reconstruction protocols of the microvasculature. In this sense, a recent study by Waelchli et al. [29] provides a detailed visualization and quantification of the 3D brain vasculature using resin-based vascular corrosion casting, scanning electron microscopy, synchrotron radiation and desktop microcomputed tomography imaging. These imaging modalities can provide a large field of view of the vascular network but at the same time low resolution. On the contrary, high resolutions are associated with a smaller field [9,30]. Micro-computerized tomography (micro-CT) is a powerful tool for visualizing large vessels but, as aforementioned, it is not capable of imaging properly the microvasculature due to the lack of resolution [31]. For this reason, its use for the microvasculature needs to be modified using additional techniques. With the aim of improving micro-CT performances, Hlushchuk et al. [32] for instance presented an innovative high-resolution micro-CT imaging of animal brain vasculature. Ghanavati et al. [33] proposed a surgical protocol for improving the surgical perfusion of cerebral blood vessels throughout the murine brain and thus obtaining more consistent cerebrovascular images by X-ray micro-CT.

An additional issue is that the cerebral tissue is opaque so that conventional light microscopy is inefficient due to the light scattering provoked by lipids [34,35]. To solve this problem and allow microscopic light to penetrate the brain tissue, several optical techniques have recently been developed. All of them are based on clearing the tissue using chemical procedures. Dodt and coworkers [36] used a mixture of benzyl alcohol and benzyl benzoate to match the refractive index of fixed tissue. However, this protocol only permitted a partial tissue clarification as the clearing solutions led to the rapid loss of fluorescent signals. In a later study, using a so-called 3D Imaging of Solvent Cleared Organs approach (3DISCO), they found that a fast optical clearing can be obtained [37]. Further studies [38,39], using different chemical approaches also achieved rapid tissue clearing encountering similar instability issues.

Tissue-clearing techniques emerged in the last decade to allow high-resolution 3D imaging of biological tissues. Numerous tissue clearing methods are currently available such as DISCO (iDISCO, uDISCO and 3DISCO) [37,40,41], CLARITY [34,42–47], and seeDB [39], among others. Most of these protocols reduce the light scattering provoked by the presence of the lipid and homogenize the RI, obtaining more transparent tissues [48]. Susaki and coworkers [35] developed a whole-brain clearing and imaging method called CUBIC (Clear, Unobstructed Brain Imaging Cocktails and Computational analysis). CUBIC is a comprehensive experimental method involving the immersion of brain samples in chemical cocktails containing aminoalcohols, which enables rapid whole-brain imaging with single-photon excitation microscopy. In parallel, they also improved

their methodology developing the so-called Advanced CUBIC clearing method. This improvement was based on hydration and extended the clearing process to several organs of a mouse, allowing high-resolution 3D imaging [49,50]. Advanced CUBIC was time consuming, had a limited efficiency for clearing organs with high pigment content and adopted the same time for different samples. For these reasons, Res et al. [48] introduced a new ultrasound processing to reduce the clearing time and proposed a new decolorization cocktail to remove pigments. With this optimization method, also called CUBIC-Plus, they enable a considerable shortening of the time acquisition of high-resolution 3D images of the lung. Pinheiro et al. [51] developed an improved clearing protocol, called CUBIC-f, for optimizing fragile samples. Hasegawa et al. [52] introduced CUBIC-kidney for kidney research applications. Based on the CUBIC methodology, Murakami et al. [53] proposed a fluorescent-protein-compatible clearing and homogeneous expansion protocol based on an aqueous chemical solution (CUBIC-X). The expansion of the brain sample allowed the construction of a point-based mouse brain atlas that allows the analysis of numerous samples providing a platform for different organs in the biomedical research, the so-called CUBIC-Atlas [54].

Notwithstanding that imaging techniques are continuously progressing, there are no specific techniques that alone are capable of providing the entire cerebral blood vessels for further reconstruction of comprehensive 3D models [9]. In general, the data obtained after the medical imaging techniques require considerable additional work before these can be treated by computer-aided design programs and computational software. An important pre-processing is for instance necessary for closing all the gaps of the acquired data, simplifying and smoothing the segments of the network that represent the vessels, avoiding noise and generating surfaces that form the limits of the computational domain [3,5,8,9,11,12]. For this reason, in the literature, idealized synthetic computational models based on mathematical algorithms are considered a valuable way to study the cerebral microvasculature. They avoid some of the limitations affecting images-based methods due to the considered microscale [9]. It is about the binary branching trees or networks that mimic the vascular bed morphology. However, the cerebral microvasculature presents for instance loops and anastomoses that cannot be taken into account using simple fractal networks [9]. Hence, simplified binary fractal trees [55–57] have been progressively more and more replaced by complex networks. These models are useful tools for different purposes. In the literature, computer methods have been often based on brain animal images due to the impossibility of invasive experimentation in humans [4,6]. Some studies have been used for interpreting optical measurements acquired in rodents [58,59]. Others were oriented to the analysis of intracellular transport phenomena on length scales not accessible to imaging methods [60,61]. Sherwin et al. [62] introduced a 1D model of a vascular network in space-time variables. Boas et al. [63] presented a symmetric binary vascular network composed by 190 segments to investigate the steady-state or transient response to specific diameter variations of the arteriolar region. Reichold et al. [28] proposed a computational methodology based on anatomical data obtained by synchrotron radiation X-Ray Tomography for simulating rat cerebral blood flow. They presented qualitative results of a fully three-dimensional intra-cortical vasculature structure modeled as a vascular graph. Lorthois and coworkers [3–6,64,65] have provided a large quantitative data focused on the microcirculation of the human cerebral cortex. Recently, they have introduced an analytical model capable of describing the coupling between arteriolar and venular trees, which were modeled using a vascular network approach and the capillary tree, modeled as a continuum porous medium. The research group of Linninger, Hartung and coworkers [2,9,13,14,16,24,66–68] has extensively worked in the microvascular architecture hemodynamics obtaining detailed information on the cerebral microcirculation inside the cerebral cortex by means of vascular networks and numerical algorithms. They analyzed the tissue metabolism coupled to micro-hemodynamics [66], and latterly, they introduced an alternative method to the binary tree for obtaining a more realistic microcirculatory network. This model was generated using Voronoi tessellation first and was later improved

by introducing novel closed networks. It finally includes an arterial and a venous tree with capillary connection synthesized with a single algorithm that allows reducing the computational costs [9].

To the best of our knowledge, there are no studies in the literature that combine tissue clearing, advanced microscopy with images treatment, geometrical reconstruction and numerical simulations. In this study, we aimed to introduce a novel protocol that combines all these techniques for obtaining detailed information about cerebrovascular cortical microcirculation. Concretely, we propose the combination of tissue clearing and advanced microscopy techniques with image treatment, geometrical reconstruction and numerical simulations. With the proposed protocol, we provided a 1D image-based computational model of the cerebral murine microvasculature that allows solving instantaneously the associated hemodynamics. Blood flow features and a quantitative evaluation of the microvascular morphology at the brain cortical territory can be predicted. In particular, different regions and depths of the BBB were considered and investigated with the aim of helping understand its microvascular functionalities and characteristics.

2. Materials and Methods

As described in the previous section, the cerebral tissue is opaque due to the presence of lipids, so conventional light microscopy is inefficient [34,35]. Hence, the lipids need firstly to be removed from this tissue for allowing the light passage without scattering or absorption, matching the refraction index (RI) between the tissue and medium. The tissue clarification is a chemical process of delipidation, decoloring and RI matching.

In this work, the mouse brain samples were treated as follows:

1. Fixation: Samples were fixed using paraformaldehyde (PFA) after transcardiacally mice perfusion and dissection before post-fixation with PFA.
2. Sectioning: Here, 500 μm thick brain slices were sectioned using a vibratome.
3. Clearing: Sections were cleared using the CUBIC protocol.
4. Staining: Delipidated sections were stained with FITC-Lectin and an arteriole-specific dye Alexa Fluor 633 hydrazide.
5. Imaging: Here, 500 μm slices were analyzed using an advanced two-photon microscopy.

Figure 1 shows the step-by-step the process followed. In the next subsections, each step is described.

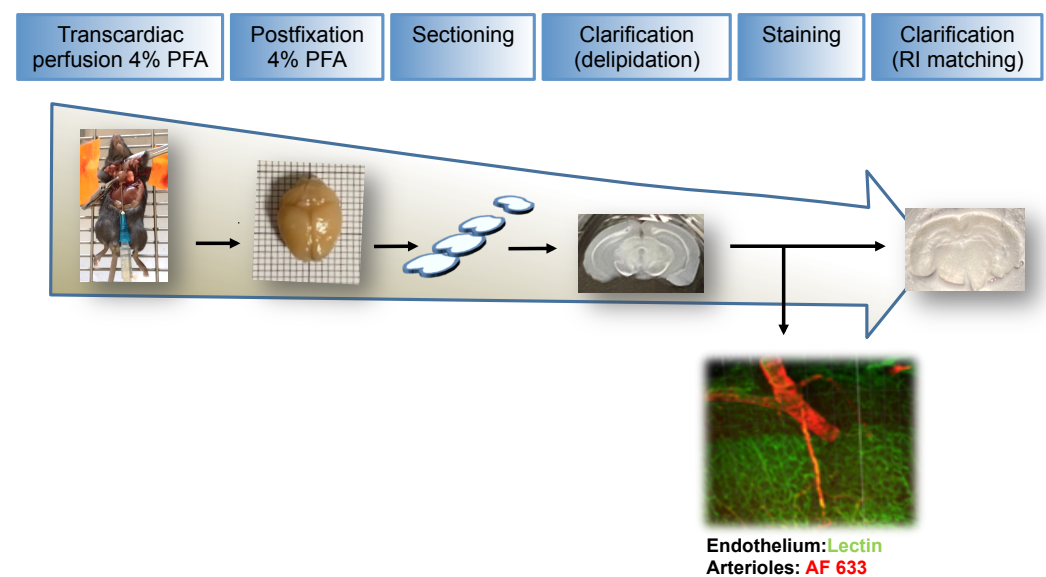


Figure 1. From mouse transcardiac perfusion to staining and cleared tissue.

2.1. Fixation, Sectioning and Tissue Optical Clearing

Specifically, all animal procedures of this study followed European and Spanish legal regulations and were performed under an ethical protocol approved by the University of Navarra Committee for Ethical Use of Laboratory Animal (076-19). Concretely, C57B6 mice were euthanized and transcardiacally perfused with PBS (pH = 7.4) and 10 mL of 4% paraformaldehyde in PBS. Mice's brains were dissected, post-fixed overnight in 4% PFA and washed with PBS. Then, 500 μm thick brain slices were sectioned using a vibratome (VT1000S, Leica, Leica Biosystems Technologies, Danaher Corporation, Washington, DC, USA) and kept in PBS solution at 4 $^{\circ}\text{C}$. Sections were cleared following the CUBIC protocol [50]. The method consists of two phases: delipidation with ScaleCUBIC Reagent-1 (urea 25 wt %, Quadrol 25 wt %, Triton X-100 15 wt % and $d\text{H}_2\text{O}$) and refractive index matching with ScaleCUBIC Reagent 2 (urea 25 wt %, sucrose 50 wt %, triethanolamine 10 wt % and $d\text{H}_2\text{O}$). The brain slices were first incubated with ScaleCUBIC Reagent-1 for 4 days at 37 $^{\circ}\text{C}$ while gentle shaking, which was followed by PBS washing for 16 h at room temperature. After that, the tissue staining was performed, and the slices were immersed in ScaleCUBIC Reagent 2 until their visualization in the microscope.

2.2. Tissue Staining

Staining of the endothelium in the brain tissue sections was performed between the first and second phases of the clearing process. To this end, delipidated sections immersed in PBS were blocked with BSA 4% and incubated with a 50 $\mu\text{g}/\text{mL}$ solution of FITC-Lectin (Sigma-Aldrich, Merck KGaA, Darmstadt, Germany, USA) during 24 h at room temperature. Finally, the sections were incubated with arteriole-specific dye Alexa Fluor 633 hydrazide solution (ThermoFisher Scientific, Waltham, MA, USA) (2 μm) for 1 h. Following the arterioles down to the capillaries in the acquired 3D volumes, we determined the areas of connection between the arterial and venous system. This allowed establishing the inlets and outlets of the computational model and hence obtaining later the correct flow direction in the simulations.

2.3. Two-Photon Excitation Microscopy

Image stacks (1 mm \times 1 mm \times 0.5 mm in size) were collected using a Zeiss LSM 880 (Carl Zeiss, Jena, Germany) equipped with a two-photon femtosecond pulsed laser (MaiTai DeepSee, Spectra-Physics, Milpitas, CA, USA), tuned to a central wavelength of 800 nm, using a 25 \times /1.8 objective (LD LCI Plan-Apochromat 25 \times /0.8, Carl Zeiss). Tiles of z-stack scan from 500 μm sections were acquired in the non-descanned mode after spectral separation and emission re-filtering using 500–550 nm and 645–685 nm BP filters for Lectin and Alexa 633 signals, respectively. In Figure 2, a lectin-stained vessels region is shown with a close-up view to a cubic sample.

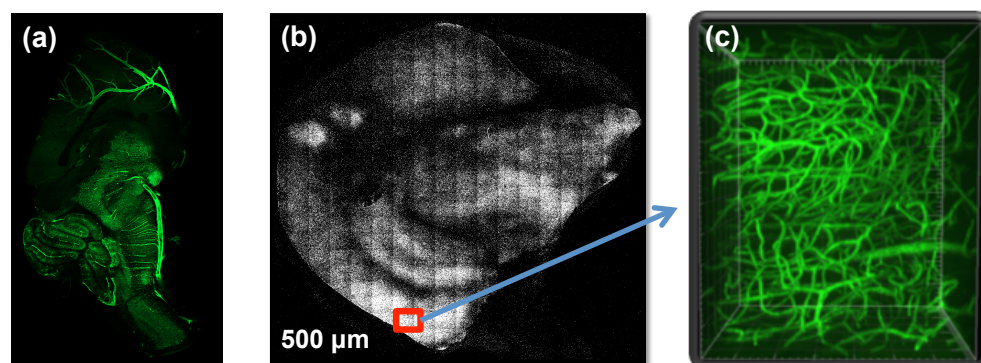


Figure 2. Tissue staining: The tissue was divided in cubic samples of 500 μm : (a) endothelial labeling with lectin; (b) cubic samples; (c) close-up view of the single cubic sample box in red in (b).

From the cubic samples represented in Figure 2b (a single region is highlighted in red), five cortical regions were selected and further used for images acquisition, geometrical

reconstruction and computational simulation, as it will be shown in the next sections. The reason why these specific regions were chosen is related to the aim of the study. The cortical regions are areas of the brain located in the cerebral cortex where the BBB is localized and thus are the target of our study because the associated microvasculature is the main filter to pharmacologic drugs. Hence, these cortical regions are of particular interest versus other brain internal areas where there is hardly any capillary network (for example, white matter situated in subcortical regions).

2.4. Image Analysis

The following procedure was applied to each vessel region obtained from the previous steps. All the image treatment was performed in MaTLAB (The MathWorks, Natick, MA, USA), using an appropriate in-house code.

Each volume was first filtered with a 3D Gaussian filter (size: $3 \times 3 \times 3$ voxels, standard deviation: $\sigma = 0.5$). Even this could lead to a possible loss of information, and the images of the present study are mainly dominated by Poisson noise; thus, we cannot neglect the presence of Gaussian noise that needs to be filtered. Then, a non-local means filter was applied to each slice [69] in the volume to reduce the Poisson noise [70] resulting from the acquisition procedure in the microscope. The vessel-like patterns were enhanced by using morphological filters with linear structuring elements, L_i , as it was performed in [71], as an adaptation of the top-hat method. In a first stage, an opening is carried out using the previously filtered volume, named as S_f , with structuring elements of varying orientation, L_i . In this way, each L_i was composed by a length of 51 voxels and a width of 1 voxel. Eight different orientations were defined in the xy -plane, i.e., horizontal plane (angular variation was $\pi/8$, i.e., 22.5°) to which eight additional angular variations were added in the z -axis direction, resulting in 64 possible structuring elements, i.e., L_i with $i = 1, \dots, 64$.

For each one of the L_i , a volume was obtained as result of an opening operation. A new volume, named S_0 , was constructed assigning to each voxel the maximum value voxel from the 64 opened volumes previously calculated, as shown in Equation (1):

$$S_0 = \max_{i=1, \dots, 64} \left\{ \gamma_{L_i} \left(S_f \right) \right\} \quad (1)$$

where γ is the opening operator. This step was finished by means of a geodesic reconstruction using S_f as a mask, obtaining the opened volume S_{op} , as shown in Equation (2):

$$S_{op} = \Gamma_{S_f}^{rec}(S_0) \quad (2)$$

where Γ is the geodesic reconstruction (opening) operator. The next step was to open S_f with the different L_i and subtract to S_{op} . Then, we added every volume calculated.

$$S_{sum} = \sum_{i=1}^{64} \left(S_{op} - \gamma_{L_i} \left(S_f \right) \right) \quad (3)$$

Once the vascular structure was enhanced, the binarizing of the volume was performed by using an adaptive threshold [72] of size 71 and a Gaussian statistic (Figure 3a,b). Finally, the biggest connected region was selected and cleaned with a morphological closing ($3 \times 3 \times 3$) and a 3D hole-filling approach [73] (Figure 3c).

Vessel Measurements

Once the volumes were binarized (Figure 3), the main geometrical features were extracted from each region. As first step, the vessel structures were skeletonized using the corresponding morphological operator by obtaining the medial axis [74,75]. In this manner, we could easily define the voxels corresponding to the vessels. Those voxels with only one neighborhood were considered as endpoints, while those others with two neighbors were treated as vessel points. Lastly, those voxels with more than two neighbors were labeled as branchpoints (usually three neighbors, but can be more). The parametrization of our vasculature structure permits breaking our vessel set into individual segments by eliminating the branchpoints that can be more easily analyzed.

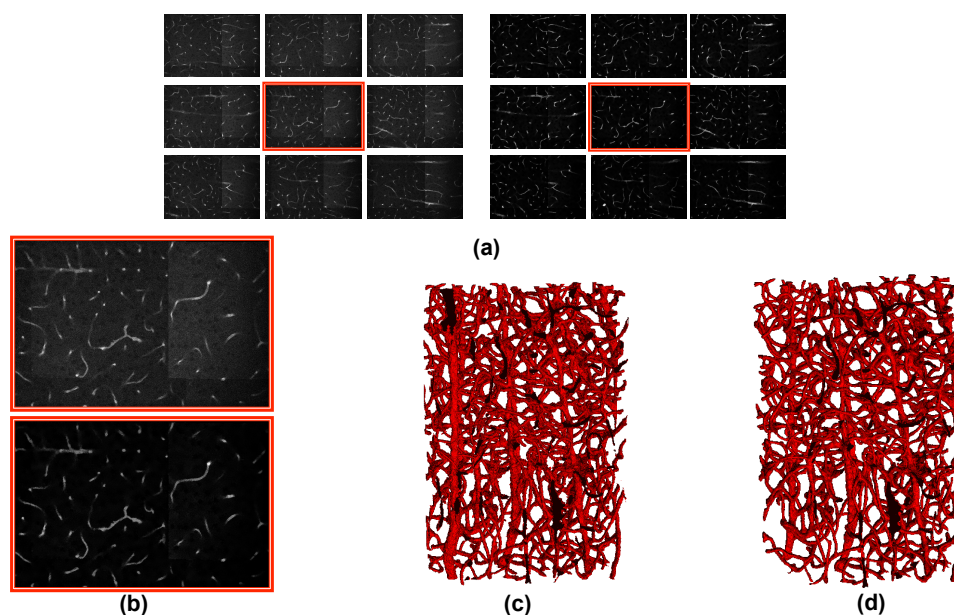


Figure 3. Image treatment: (a) Original images (left) and result of filtering (right). (b) Zoomed versions extracted from (a). Original slice (up), filtered slice (down). (c) Segmented volumen. (d) Result after artifacts erasing.

Regarding each segment, knowing the voxel size, it was possible to calculate some shape-related characteristics such as the longitude, the curvature or the tortuosity of the segment. Using the vessel set volume and the medial axis voxels data, we also calculated the radius for every skeleton voxel and then computed the mean radius for each segment. Once all the structures were parameterized, we straightforwardly constructed 1D models of the five vessel regions in which each voxel and segment are characterized for further analyses. A final representative model is depicted in the Figure 3d).

2.5. One-Dimensional (1D) Modeling

2.5.1. Governing Equations

The computational models of the previously created geometries were programmed in MaTLaB, and they were based on the hemodynamic network developed by A. R. Pries and T. W. Secomb [76]. In the literature, it is worldwide known that in microvascular networks, the velocities achieved by plasma and red blood cells (RBCs) are very low (60–1 mm/s) [77], translating into a very low Reynolds number ($Re < 0.001$ for all the analyzed regions) and leading to a laminar capillary flow. Hence, inertial forces have less influence than viscous forces. This fact, in addition with a low Womersley number ($Wo < 0.01$) indicating that the flow can be considered as no pulsatile, enabled a simplification of the Navier–Stokes equation into the Stokes equations (Equation (4)). As a result, we simplified the flow in the capillary bed as a ratio of the pressure drop in every capillary and its hydraulic resistivity:

$$\mu \nabla^2 \mathbf{v} + \nabla p = 0 \quad (4)$$

The model handled in this study, after its processing, became a 3D network built from nodes and cylindrical segments in which all the constitutive equations were solved. This model was composed by a collection of interconnected nodes and segments of the BBB microvascular geometry. In this vascular network, the nodes represented locations where vessels bifurcated or ended, and the segments represented the vessels. Each node was defined by coordinates and each segment was defined by nodes and diameters. Every segment was then divided into several intermediate segments, making possible the use of tortuous vessel length instead of simplifying the vessels as straight lines between two

end points (Figure 4). Hence, the total length of the vessel was obtained as the sum of the lengths of consecutive intermediate segments (Equation (5), Figure 4).

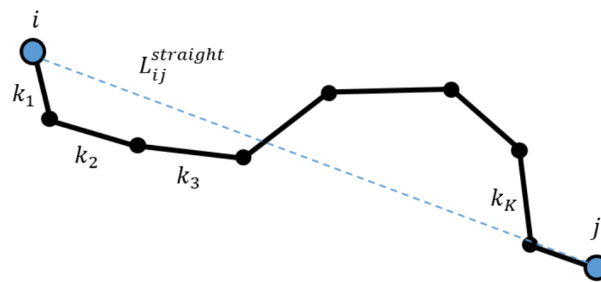


Figure 4. Schematic representation of the segments subdivisions.

$$L_{ij}^{total} = \sum_i^k L_{ij,k} \tag{5}$$

where L_{ij} was the total segment length divided by k intermediate segments. Initially, the mass flow entering a node was the same as the outflow of this node, fulfilling the continuity equation in every geometry node (Equation (6)).

$$\nabla \cdot \mathbf{v} = 0 \Rightarrow \dot{\mathbf{m}}_{in} = \sum \dot{\mathbf{m}}_{out} \tag{6}$$

On the other hand, the blood flow (Q) in every capillary segment was calculated as shown in Equation (7):

$$Q_{ij} = \frac{\Delta p_{ij}}{R_{ij}} \tag{7}$$

where Δp represented the pressure drop between the defining nodes of the segment ij and R represented the flow resistance of segment ij , given a cylindrical shape, which was calculated using the Hagen–Poiseuille Law (Equation (8)):

$$R_{ij} = \frac{128\mu_{ij}L_{ij}}{\pi D_{ij}^4} \tag{8}$$

The flow resistance of a segment R_{ij} depends on the diameter of the segment D_{ij} and on its length L_{ij} . In this study, the tortuous length of each vessel was taken into account instead considering only straight segments adding the tortuosity evaluated during the images’ treatment. The flow resistance depends on the blood viscosity of the segment μ_{ij} , which varies considerably between segments due to the Fahraeus–Lindqvist effect. As known, the latter is caused by the biphasic nature of the blood and the small dimensions of the capillaries [78]. The effective viscosity μ_{eff} was calculated using the in vivo empirical description made by A. R. Pries [78]. This set of empirical equations takes into account the effects of the biphasic nature of the blood in the capillary bed and calculates its effective viscosity given a vessel diameter D , velocity and hematocrit H_D as follows:

$$\mu_{ij} = \mu_{ij}^{rel} \cdot \mu_{plasma} \tag{9}$$

$$\mu_{ij}^{rel} = \left[1 + (\mu_{0.45} - 1) \cdot \frac{(1 - H_D)^C - 1}{(1 - 0.45)^C - 1} \left(\frac{D}{D - 1.1} \right)^2 \right] \cdot \left(\frac{D}{D - 1.1} \right)^2 \tag{10}$$

$$\mu_{0.45} = 6 \cdot e^{-0.085D} + 3.2 - 2.44 \cdot e^{-0.06D^{0.45}} \tag{11}$$

$$C = 0.8 + e^{-0.075D} \cdot \left(-1 + \frac{1}{1 + 10^{-11} \cdot D^{12}} \right) + \frac{1}{1 + 10^{-11} \cdot D^{12}} \tag{12}$$

The hematocrit distribution in the bifurcations of the geometry was calculated using the phase separation law established by A. R. Pries and T. W. Secomb [76]. This law contains a set of empirical equations that define the hematocrit distribution in a bifurcation knowing

the hematocrit in the mother branch and the flow and diameters of the daughter branches (Equations (13)–(15)):

$$FQ_E = 0, \text{ if } FQ_B \leq X_0 \tag{13}$$

$$\text{logit}_{FQ_E} = A + B \text{logit} \left[\frac{FQ_B - X_0}{1 - 2X_0} \right], \text{ if } X_0 \leq FQ_B \leq 1 - X_0 \tag{14}$$

$$FQ_E = 1, \text{ if } 1 - X_0 \leq FQ_B \tag{15}$$

where FQ_B was the fractional blood flow in the daughter branch (ratio of the blood flow of the daughter branch and the mother branch) and FQ_E was the fractional erythrocyte flow in the daughter branch (ratio of the erythrocyte flow of the daughter branch and the mother branch). The relationship between erythrocyte flow, blood flow and the segment hematocrit was obtained using the following equation:

$$Q_E = Q_B \cdot H_D \tag{16}$$

The parameters A , B and X_0 were obtained as follows:

$$A = -13.29 \cdot \left(\frac{\frac{D_A^2}{D_B^2} - 1}{\frac{D_A^2}{D_B^2} + 1} \right) \cdot \frac{1 - H_D}{D_F} \tag{17}$$

$$B = 1 + \frac{6.98(1 - H_D)}{D_F} \tag{18}$$

$$X_0 = \frac{0.964(1 - H_D)}{D_F} \tag{19}$$

where D_A and D_B were the diameters of the daughter branches and D_F and H_D were the diameter and hematocrit of the mother branch.

2.5.2. Boundary Conditions

It is widely known that one of the most challenging parts in simulating microvascular networks is to establish the conditions in all the in/outflows that appear in the limits of the computational domain. These conditions are necessary for the solution of the 1D equations that describe the blood flow inside the microvasculature. In particular, flow, pressure and hematocrit conditions must be set and, depending on their values, the calculations predict accurate (or less accurate) physiologically meaningful results. In this work, as experimental measurements were not possible in murine brains, some approximations were taken, and literature data were adopted. Different authors used various solutions to this problem [5,24,76,77]. In this work, the solution presented by Lorthois et al. [5] was chosen, as it was simple and fast to implement and achieved valid predictions, comparing the obtained results. The used set of boundary conditions are taken from [77,79] and are described below:

- (a) Pressures were imposed at the inlet and outlets. With that, there was no need to know the flow direction in all in- and outflows respectively, as the flow direction in the segments adjusted to fulfill the pressure boundary conditions.
- (b) Boundary nodes (1 segment nodes) inside the geometries limits were assigned with a zero flow condition and with zero hematocrit. These nodes show the presence of *broken* vessels inside the geometry that could be produced during the segmentation. It is important to notice that these vessels have no physiological meaning but need to be treated.
- (c) Three different sets of pressure boundary conditions were assigned depending on the segment to which the boundary node was attached to: venule, arteriole or capillary:
 1. At the arterial inflow, a pressure of 50 mmHg was given. The arterial pressure outflow was set to 40 or 45 mmHg depending on its nearness to the inflow. With that, the risk of a short circuit was eliminated.

2. At the venular outflows, a pressure of 10 mmHg was given.
3. In the capillary in/outflows, two cases were studied, following Lorthois and coworkers [5]:

Case 1: Zero flow condition: Flow is set to zero in all the capillary outflows. In this case, the flow goes from the arterial inlet passing through the whole geometry until it reaches a venular outlet. As reported [5], this condition would underestimate the flow in the geometry as it isolates it from its virtual neighbors.

Case 2: Constant pressure condition: A constant capillary boundary pressure was calculated so that the net capillary flow (the sum of the flow in all the inlets and outlets) was zero; thus, everything that enters through the arterioles exits through the venules. In other words, this pressure was adjusted such that the total flow entering the arteriolar network was the same as the total flow entering the venular network. In this way, the net flux to all the boundary capillary segments was zero. As a consequence, the net flux leaving the studied brain region through capillaries to supply neighboring areas was exactly compensated by the net flux arriving from neighboring areas through capillaries. As shown in the literature, this condition forces the flux lines to be perpendicular to the ends of the computational domain, maximizing the exchanges of fluid with the neighboring region. For this reason, this condition overestimates the flow in the geometry as it maximizes the flow exchange between the region itself and its virtual neighbors. [64].

- (d) The boundary hematocrits values were set 0.45 at the arterial inlets, 0.4 at the arterial outlets, 0.2 at the venular outlets and a random value between 0.2 and 0.6 for the rest of the capillary boundary nodes, mimicking the chaotic and heterogeneous nature of this variable in the capillary beds [5,64].

The influence of imposing zero flow or a constant pressure at the capillary outlets was found to be limited. Similar results were found also by [5]. Finally, we chose the second option (constant pressure condition), as the first one (zero flow) tended to isolate the volume of the considered capillary regions.

3. Results

This paper focuses on the image-based circulatory network of the BBB and shows the versatility of the presented methodology for analyzing up to five cortical regions of the murine brain vasculature. The main purpose of the framework is to introduce a consistent methodology for elucidating the murine microvascular hemodynamics and other functions related to the BBB. The presented synthetic anatomical networks are easy to be treated using 1D hemodynamics. In this section, we illustrate some computational results in terms of flow, pressure, hematocrit and endothelial shear stress. The results took a few CPU minutes to be obtained and required around 20 GB of memory in serial execution on a HP Z440 Intel Xeon computer.

The network geometries are represented in Figure 5 and are colored by the values of the vessels diameter. These regions considered one inlet each but a different number of outlets, different vessel densities, mean diameters, curvatures and tortuosities and the number of bifurcations among other morphological differences. As visible from the figure, the morphology of the five regions is widely different. Of course, these topologies strongly influence the flow patterns and the associated nutrient transport in the surrounding tissue. For these reasons, it is relevant to show the different statistics associated to the flow simulations of the five cerebral regions. Frequency distributions of vessel diameters, length, surface area and volume that characterize the five networks reconstructed using the presented algorithm are shown in Figure 6. The geometries show a very good correlation in terms of segment diameters (in μm) and lengths (in μm), surface area (in μm^2) and

total vascular volume (in μm^3) distributions, as shown in Figure 6 where the cumulative distribution function (CDF) of these variables is depicted. The presented curves match well the shape and order of magnitude of those presented by Linninger and coworkers [9] which were obtained using a mathematical synthesis of the cortical circulation for a whole mouse brain. The obtained relations between the frequency of appearance and diameters, lengths, surfaces and volumes are in agreement also with those found by other authors, showing that the used geometries are suitable for further use in the numerical simulations of the microvascular blood flow. This comparison ensures that our image-based modeling presents anatomically consistent microvasculature.

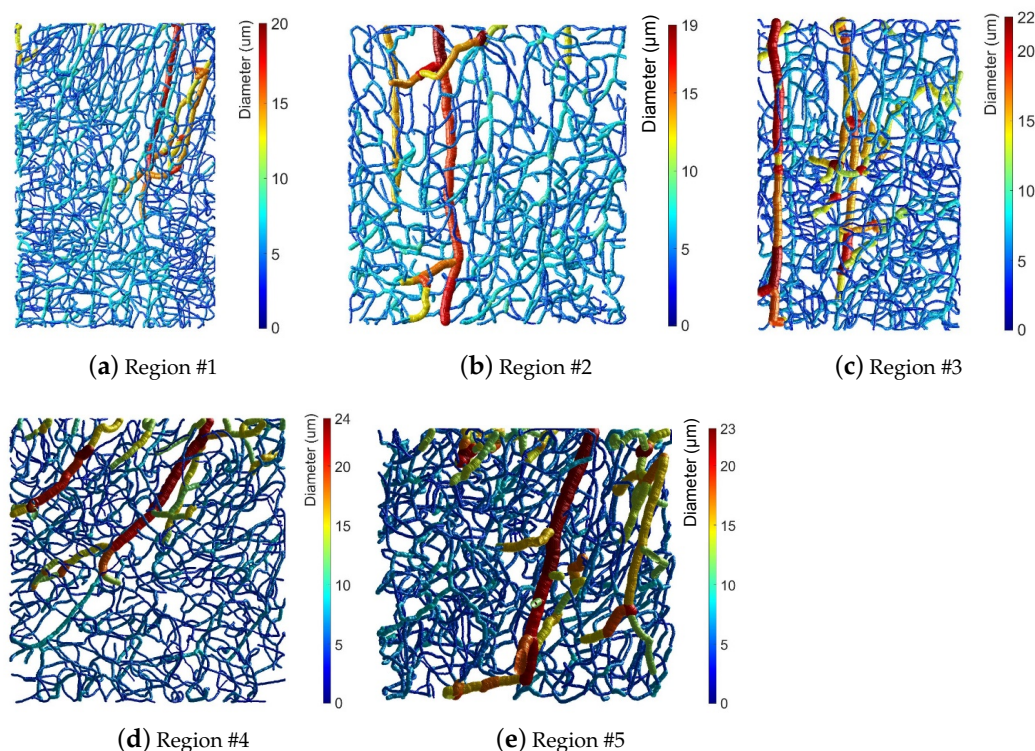


Figure 5. Morphology of the 5 cerebrovascular regions of the murine cortex considered in this study. The heat map represents by color the distribution of the value of the diameters within the microcirculatory synthetic network.

Additionally, the framework is capable of controlling the number of arteries and bifurcations and all the associated geometrical features that are quantified in the image data and included in the synthetic model. Previously published capillary networks use only straight segments with cylindrical shape for describing the microvasculature. However, real networks present curvature and tortuosity. Both variables were measured here directly from the images. In particular, the tortuosity was computed using the metric SOAM described by Bullit et al. [80]. We imposed the tortuosity measured directly from the images for mimicking imaged networks. Its CDF is depicted in the Figure 6e). Moreover, we provided a venous connection between arteriolar and capillary regions thanks to the double staining. Previous studies habitually neglected curvature and tortuosity, presenting straight vessel instead, and only a few consider venous drainage [9].

The five different geometries that have been analyzed in this work and depicted in Figure 5 are defined by the parameters summarized in Table 1.

Table 1. Morphological properties of the 5 considered cortical regions.

Region	Nodes	Boundary Nodes	Segments	Dimensions (μm)
#1	1250	210	1561	$698 \times 459 \times 310$
#2	751	136	932	$466 \times 432 \times 207$
#3	968	134	1265	$559 \times 365 \times 318$
#4	948	198	1164	$517 \times 532 \times 220$
#5	999	72	1292	$508 \times 383 \times 345$

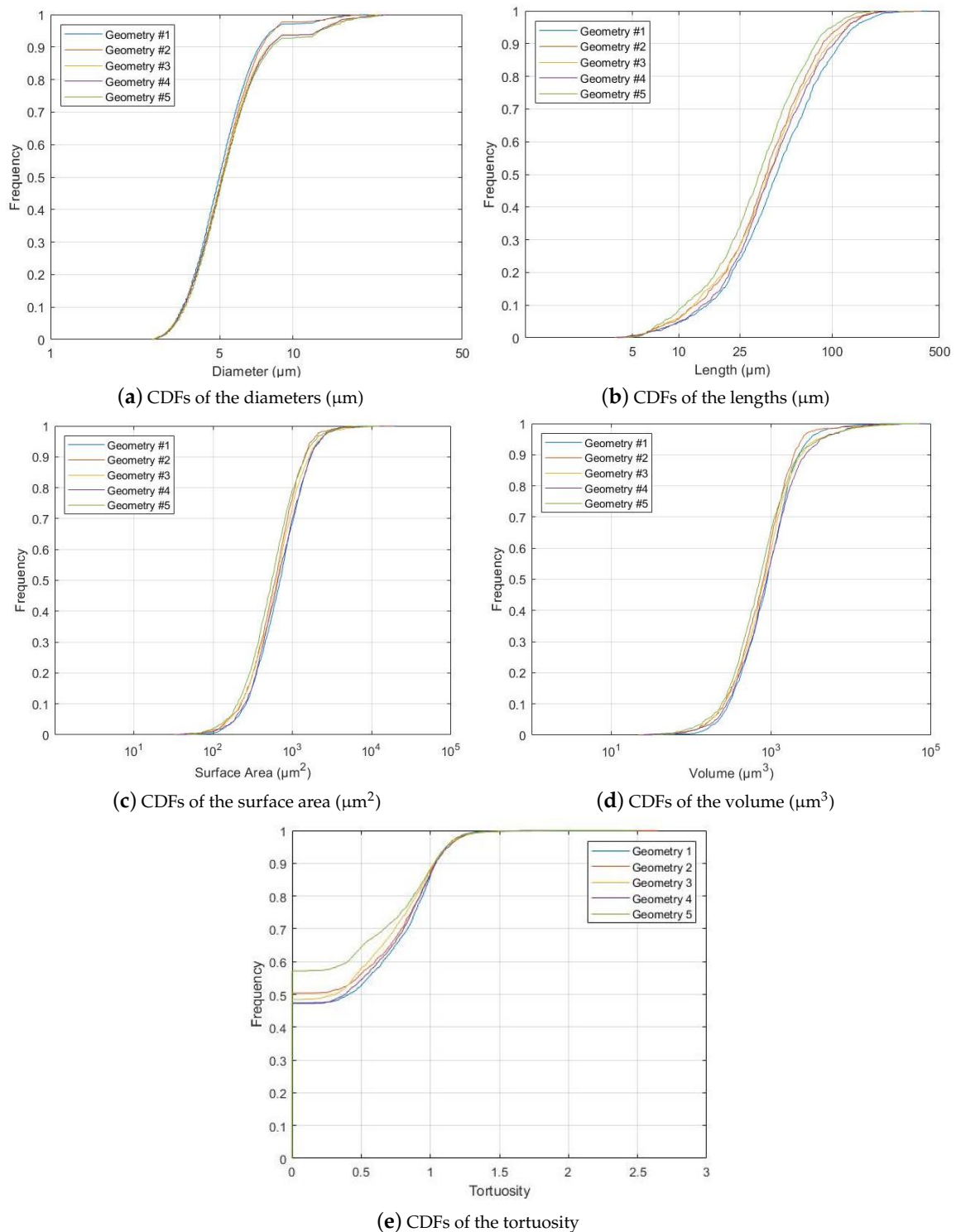


Figure 6. Statistical analysis of the considered regions: cumulative distribution functions of diameters (a), lengths (b), surface areas (c), volumes (d) and tortuosity (e).

The blood flow distributions of the five regions is depicted in Figure 7 in logarithmic scale for enhancing differences within the vessel segments. As the regions are of different size and present important morphological differences, the maximum and minimum of the scale is different for each geometry. The results of the simulations showed that a peak blood flow of 437.33 nL/min was found in Geometry #4, while the minimum blood flow was 99.65 nL/min and belonged to Geometry #3. Summarizing, we found a mean blood flow of 268.49 ± 168.84 nL/min. This value differed from the values by Hurtung and coworkers [24]. However, even though they have found a maximum blood flow of around 780 nL/min, they considered wider regions and scales than the ones used in this work. Of course, the comparison can be only performed qualitatively because it is about different samples with variable morphologies. The important variability of the blood flows found in the present work can be explained by the geometrical differences presented by the 5 regions. In some of them, the feeding arteriolar branch present 'shortcuts' to the outlets, having a preferential flow path of little resistance and increasing the blood flow. This happens, for example, in Geometries #4 and #5, indicated in Figure 7. Furthermore, there are slight differences in the feeding arteriolar trunk diameters, varying from 17.24 μm in Geometry #1 to 22.62 μm in Geometry #5, for instance. This causes less flow resistance for the same pressure loss between inflow and outflow, leading again to an increase of the blood flow.

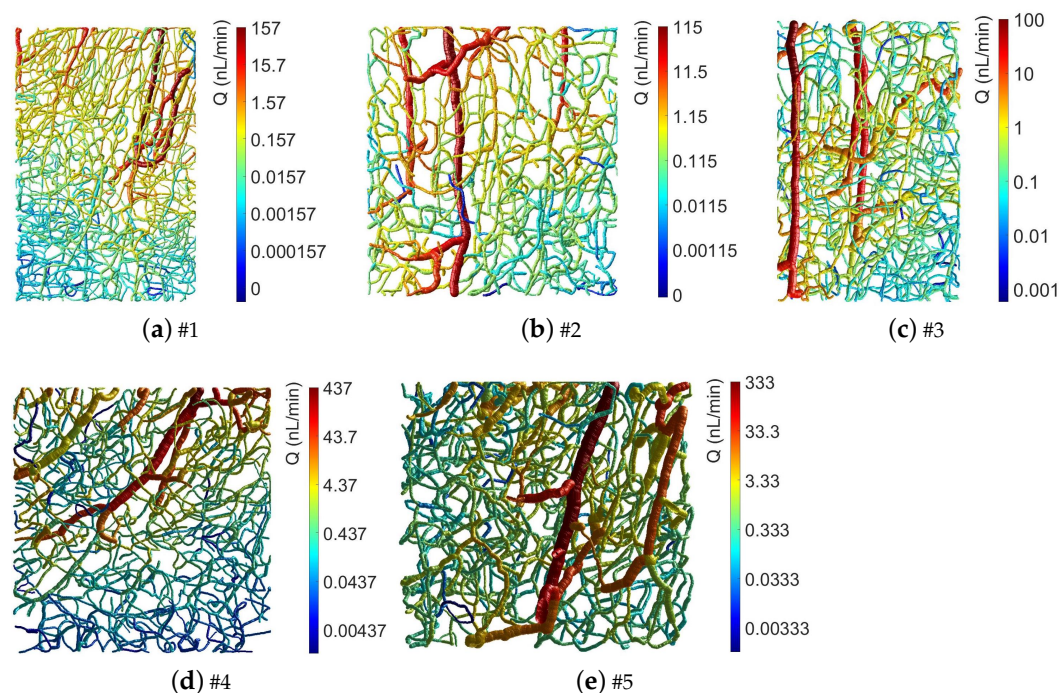


Figure 7. Computed blood flow (in [nL/min]) within the 5 cerebrovascular regions of the murine cortex. The heat map (in logarithmic scale) represents by colors the average blood flow distribution within the microcirculatory synthetic network.

Figure 8 shows the hematocrit distribution within the five regions. Initially, a maximum hematocrit of 80% has been set for any segment. The obtained distributions, as visible in the figure tend to be chaotic in all the regions. This happens because of the used geometries, as this distribution mostly depends on the asymmetry of the bifurcations inside the models due to the nature of the blood. As can be found in the literature, the hematocrit distribution differs from realistic to synthetic, symmetric, binary tree geometries. In these geometries, the hematocrit distribution is in fact mostly homogeneous [24]. The variations seen in Figure 8 are the result of the morphology of the five considered regions. The position of the venous drainage in the geometries can affect hugely the hematocrit distribution, as this is the location where the flow exits and where convergent bifurcations appear. Additionally, there are also some locations in the geometries where divergent

bifurcations appear, leading to a decrease of the hematocrit in the segments until it reduces even to 0%, as seen for instance in Geometry #1. On the other hand, in all geometries, some vessels with slightly high hematocrit values can be seen. These increases of hematocrit depends both on the segment diameter and on the feeding segment hematocrit, being usually convergent bifurcations.

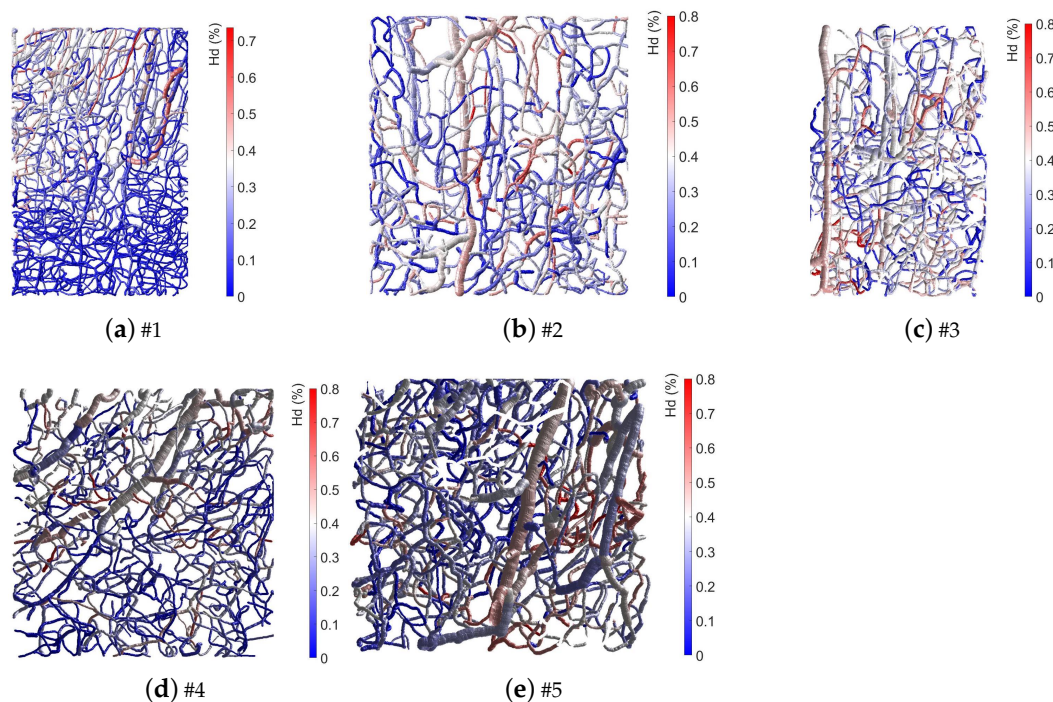


Figure 8. Computed hematocrit (in [%]) within the 5 cerebrovascular regions of the murine cortex. The heat map represents by colors the hematocrit percentage per segment within the microcirculatory synthetic network.

4. Discussion

The brain is the most complex organ of humans, but despite the extensive work dedicated in recent decades, still little is known about its functionalities, including the anatomy and the hemodynamics of its vasculature in comparison with all the other organs [81]. Several studies have attempted to describe the microvasculature structure and anatomical variations in the cerebral surface region often comparing humans and rats that present many similarities but also differences [82]. We have proposed a comprehensive framework based on tissue clarification, advanced microscopy and image treatment aimed at the analysis of the murine microvasculature that is feasible to be applied to humans. Through a mathematical algorithm, specific regions or even the entire murine brain geometry can theoretically be created for the analysis of its hemodynamics. The reconstruction of the entire anatomy from image data is difficult to be obtained as patient-specific data have a limited spatial resolution [9]. For this reason, the combination of anatomical images, from the tissue clarification to the obtention of 3D geometries, and mathematical modeling using advanced algorithms that allow the analysis of a consistent circulatory network is an efficient strategy, and it is the standard methodology in the literature. The advantage of the synthetic network is that it can be used for different purposes, for example for the simulation of blood flow and nutrients transport phenomena that can mimic the 3D vasculature. These simulations can cover regions of the in vivo data sets where imaging data are not consistent, as we have discussed in the Section 2.5.1 or regions not reconstructed [9]. Alternatively, the use of mathematical networks could also be capable of complementing real anatomical data serving as boundary conditions for 3D realistic anatomical microcirculatory models. The 1D modeling can be attached to 3D models replacing the limits of the computational

vascular domains and can be used for applying the boundary conditions as elucidated by Linninger and coworkers [9]. Fractal networks have been often used in this sense for large and small arteries as well as for the cerebral vasculature [83–85].

In the past decade, synthetic vascular models have offered more and more an alternative to purely image-based approaches [65,81,86,87]. Unfortunately, binary trees can only approximate the real microvasculature because they only bifurcate in one direction and cannot take into account loops. For this reason, more recently, other authors start creating more complex vascular structures that could include anastomoses improving previous findings [9]. Our work demonstrated that the presented methodology offers such morphological structures as the obtained synthetic models faithfully represent the imaged cortical regions.

At the same time, researchers have progressively proposed improved mathematical algorithms providing increased models complexity yet providing accurate brain data-based networks. An example is the synthetic model introduced by Linninger et al., which simulates the cortical blood supply in a section of the human cortex. They provided a computational method for building realistic microcirculatory beds using Voronoi tessellation [66]. Due to the high computational costs, they later further extended this model using a single algorithm including arterial and venous trees with capillary connection [9]. Another example is the algorithm developed by Su et al. for creating a set of networks based on experimental statistics to bypass the complexities to reconstruct a cerebral microvascular network from real brain tissue data [81].

The principles of the modeling proposed in the present work are similar to those introduced by other studies in the literature [63]. The cerebral vasculature is represented by a network of bifurcating cylinders that provide a resistance to flow according to the Stokes equations. The proposed mathematical model was further used for studying the hemodynamic in the brain for showing the application of the developed methodology. Some computational results regarding the blood flow, the hematocrit and the endothelial shear stress distribution have been presented (see Figures 7–9) and demonstrate the feasibility, the utility and versatility of the presented framework. With the proposed framework, it is also possible to have a consistent quantification of the vascular morphology, providing data of the number of bifurcations, tortuosity, surface, vessel length and diameter, volume and volume density that can be used for characterizing the vascular structure and its functionality (see Figure 6). It is widely known that the neuronal tissue varies with the depth of the cerebral cortex so that the presented results may be used to help elucidate the relationship of the flow, pressure and shear stress characteristics with the depth in 1D realistic vascular networks as studied by other authors but still not yet fully understood [77]. The computational results support the hypothesis already diffused in the literature that the flow field and the hematocrit distribution are highly heterogeneous in the microvasculature, suggesting that the oxygen and nutrients brain regulations depend on the cortical layer [25,77].

The presented simulations are based on a real anatomical data so that reconstructed geometries are controllable. However, the results leads to 1D flow and average values of velocity, WSS and other variables that approximate the real cerebrovascular hemodynamics. Of course, synthetic models are based on simplified geometries and simplified hemodynamic constraints as a boundary condition so that the resulting hemodynamic features are simplified as well [9]. For this reason, the results obtained in this study were compared with published results for demonstrating the consistency and robustness of the presented tool. Unfortunately, currently, an *in vitro* or an experimental validation is not feasible. Nevertheless, as stated in the literature [9], simplified hemodynamic models used in combination with synthetic vascular networks do not preclude rigorous blood flow simulations. In this sense, the advantage of the presented model is that one can control all geometrical parameters and preview the results in real time. Additionally, as explained before, the presented framework is feasible to be more and more complicated adding or improving model details and additional specific conditions. In conclusion, although it includes some simplifications, the presented mathematical model which incorporates anatomic-based

morphometric properties can potentially be used for addressing open questions regarding healthy and diseased cortical blood flow in the cerebral microvasculature.

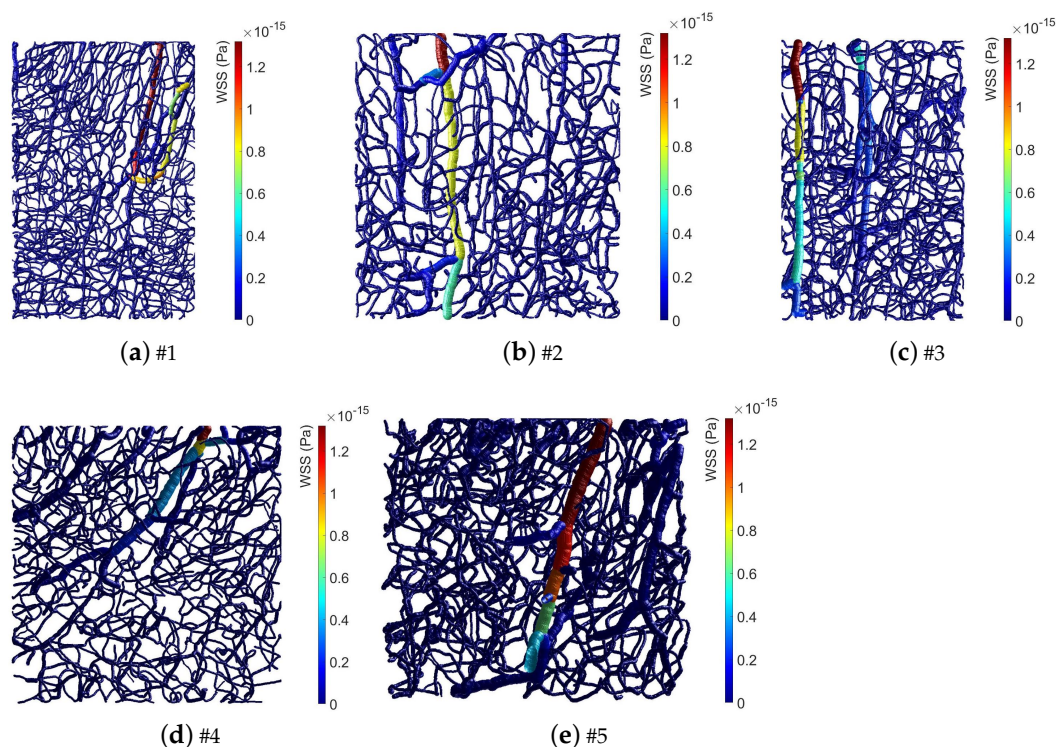


Figure 9. Computed endothelial shear stress of the 5 cerebrovascular regions of the murine cortex. The heat map represents by colors the average value of the shear stress per segment within the microcirculatory synthetic network.

5. Conclusions

We presented a comprehensive numerical tool for the generation and analysis of image-based artificial vascular networks. This novel methodology is based on tissue clearing, two-photon microscopy, image acquisition and treatment and 1D computational modeling. We have analyzed five cortical regions showing that the framework is capable of correctly synthesizing the cortex microvasculature from a morphological and hemodynamical point of view. Furthermore, the tissue clearing-based methodology is flexible and it can be applied to human brains that have bigger sizes. In contrast with previous studies, the methodology includes a physiological connection to the venous drainage and some morphological features such as curvature and tortuosity. The obtained results are in line with the literature so that the presented mathematical model allows studying the healthy cerebral microvasculature for computing the hemodynamics of the BBB. Lastly, the presented methodology is feasible to be applied as well to pathological cerebral microvasculature helping understanding the role of the hemodynamics in neurodegenerative diseases.

Author Contributions: Conceptualization, N.R., C.O.-d.-S., A.V. and M.M.; methodology, C.E., A.U., E.R.-d.-M., A.O., I.C.-D., N.R., A.V. and M.M.; software, S.M.; formal analysis, S.M., A.S., A.U., E.R.-d.-M. and A.O.; investigation, S.M., A.S., C.E., A.U., E.R.-d.-M., A.O., I.C.-D., N.R., C.O.-d.-S., A.V. and M.M.; resources, N.R., C.O.-d.-S., A.V. and M.M.; data curation, A.S., C.E., A.U., E.R.-d.-M., A.O., I.C.-D. and A.V.; writing—original draft preparation, S.M., A.S., I.C.-D. and M.M.; writing—review and editing, I.C.-D., N.R., C.O.-d.-S., A.V. and M.M.; visualization, S.M., A.S. and A.V.; supervision, N.R., C.O.-d.-S., A.V. and M.M.; project administration, N.R., C.O.-d.-S. and M.M.; funding acquisition, N.R., C.O.-d.-S. and M.M. All authors have read and agreed to the published version of the manuscript.

Funding: The study is financially supported by the Economic Department of the Navarre Government through the research project 0011-1411-2020-000025 (3D3B-AVATAR).

Institutional Review Board Statement: The study was conducted according to the guidelines of the Declaration of Helsinki, and approved by the Ethics Committee of the University of Navarra (076-19, 9 October 2019).

Data Availability Statement: Some of the presented data could be available from the corresponding author on reasonable request.

Acknowledgments: The support of the Instituto de Salud Carlos III (ISCIII) through the CIBER-BBN initiative is gratefully acknowledged.

Conflicts of Interest: The authors declare no conflict of interest.

References

- Boileau, E.; Nithiarasu, P.; Blanco, P.J.; Muller, L.O.; Eikeland Fossan, F.; Hellevik, L.R.; Donders, W.P.; Huberts, W.; Willemet, M.; Alastruey, J. A benchmark study of numerical schemes for one-dimensional arterial blood flow modelling. *Int. J. Numer. Methods Biomed. Eng.* **2015**, *31*, e02732. [[CrossRef](#)]
- Park, C.S.; Hartung, G.; Alaraj, A.; Du, X.; Charbel, F.T.; Linninger, A.A. Quantification of blood flow patterns in the cerebral arterial circulation of individual (human) subjects. *Int. J. Numer. Methods Biomed. Eng.* **2020**, *36*, e3288. [[CrossRef](#)] [[PubMed](#)]
- Cassot, F.; Lauwers, F.; Fouard, C.; Prohaska, S.; Lauwers-Cances, V. A novel three-dimensional computer-assisted method for a quantitative study of microvascular networks of the human cerebral cortex. *Microcirculation* **2006**, *13*, 1–18. [[CrossRef](#)] [[PubMed](#)]
- Lauwers, F.; Cassot, F.; Lauwers-Cances, V.; Puwanarajah, P.; Duvernoy, H. Morphometry of the human cerebral cortex microcirculation: general characteristics and space-related profiles. *Neuroimage* **2008**, *39*, 936–948. [[CrossRef](#)] [[PubMed](#)]
- Lorthois, S.; Cassot, F.; Lauwers, F. Simulation study of brain blood ow regulation by intra-cortical arterioles in an anatomically accurate large human vascular network: Part I: methodology and baseline flow. *NeuroImage* **2011**, *54*, 1031–1042. [[CrossRef](#)]
- Lorthois, S.; Cassot, F.; Lauwers, F. Simulation study of brain blood flow regulation by intra-cortical arterioles in an anatomically accurate large human vascular network. Part II: Flow variations induced by global or localized modifications of arteriolar diameters. *NeuroImage* **2011**, *54*, 2840–2853. [[CrossRef](#)]
- Schmid, F.; Reichold, J.; Weber, B.; Jenny, P. The impact of capillary dilation on the distribution of red blood cells in artificial networks. *Am. J. Physiol.—Heart Circ. Physiol.* **2015**, *308*, H733–H742. [[CrossRef](#)]
- Schmid, F.; Tsai, P.S.; Kleinfeld, D.; Jenny, P.; Weber, B. Depth-dependent flow and pressure characteristics in cortical microvascular networks. *PLoS Comput. Biol.* **2017**, *13*, e1005392. [[CrossRef](#)]
- Linninger, A.; Hartung, G.; Badr, S.; Morley, R. Mathematical synthesis of the cortical circulation for the whole mouse brain-part I. theory and image integration. *Comput. Biol. Med.* **2019**, *110*, 265–275. [[CrossRef](#)]
- Kidoguchi, K.; and T. Mizobe, M.T.; Koyama, J.; Kondoh, T.; Kohmura, E.; Sakurai, T.; Yokono, K.; Umetani, K. In vivo X-ray angiography in the mouse brain using synchrotron radiation. *Stroke* **2006**, *37*, 1856–1861. [[CrossRef](#)]
- Fang, Q.; Sakadžić, S.; Ruvinskaya, L.; Devor, A.; Dale, A.M.; D, A.B. Oxygen Advection and Diffusion in a Three Dimensional Vascular Anatomical Network. *Opt. Express*. **2008**, *16*, 17530–17541. [[CrossRef](#)]
- Tsai, P.S.; Kaufhold, J.P.; Blinder, P.; Friedman, B.; Drew, P.J.; Karten, H.J.; Lyden, P.D.; Kleinfeld, D. Correlations of neuronal and microvascular densities in murine cortex revealed by direct counting and colocalization of nuclei and vessels. *J. Neurosci.* **2009**, *29*, 14553–14570. [[CrossRef](#)]
- Gould, I.G.; Linninger, A.A. Hematocrit Distribution and Tissue Oxygenation in Large Microcirculatory Networks. *Microcirculation* **2015**, *12*, 1–18. [[CrossRef](#)]
- Gould, I.G.; Tsai, P.; Kleinfeld, D.; Linninger, A. The capillary bed offers the largest hemodynamic resistance to the cortical blood supply. *J. Cereb. Blood Flow Metab.* **2017**, *37*, 52–68. [[CrossRef](#)]
- Gagnon, L.; Smith, A.F.; Boas, D.A.; Devor, A.; Secomb, T.W.; Sakadžić, S. Modeling of Cerebral Oxygen Transport Based on In vivo Microscopic Imaging of Microvascular Network Structure, Blood Flow, and Oxygenation. *Front. Comput. Neurosci.* **2016**, *10*, 82. [[CrossRef](#)]
- Hartung, G.; Badr, S.; Moeini, M.; Lesage, F.; Kleinfeld, D.; Alaraj, A.; Linninger, A. Voxelized simulation of cerebral oxygen perfusion elucidates hypoxia in aged mouse cortex. *PLoS Comput. Biol.* **2021**, *17*, 1008584. [[CrossRef](#)]
- Chen, Q.; Jiang, L.; Li, C.; Hu, D.; Bu, J.; Cai, D.; Du, J. Haemodynamics-driven developmental pruning of brain vasculature in zebrafish. *PLoS Biol.* **2012**, *10*, e1001374. [[CrossRef](#)]
- Blumers, A.L.; Yin, M.; Nakajima, H.; Hasegawa, Y.; Li, Z.; Karniadakis, G.E. Multiscale parareal algorithm for long-time mesoscopic simulations of microvascular blood flow in zebrafish. *Comput. Mech.* **2021**, *68*, 1131–1152. [[CrossRef](#)]
- Roustaie, M.; In Baek, K.; Wang, Z.; Cavallero, S.; Satta, S.; Lai, A.; O'Donnell, R.; Vedula, V.; Ding, Y.; Marsden, A.L.; et al. Computational simulations of the 4D micro-circulatory network in zebrafish tail amputation and regeneration. *J. R. Soc. Interface* **2022**, *19*, 29210898. [[CrossRef](#)]

20. Anbazhakan, S.; Rios Coronado, P.E.; Sy-Quia, A.N.L.; Seow, A.; Hands, A.M.; Zhao, M.; Dong, M.L.; Pfaller, M.; Raftrey, B.C.; Cook, C.K.; et al. Blood flow modeling reveals improved collateral artery performance during the regenerative period in mammalian hearts. *Nat. Cardiovasc. Res.* **2022**, *1*, 775–790. [[CrossRef](#)]
21. Ronellenfitch, H.; Katifori, E. Global optimization, local adaptation, and the role of growth in distribution networks. *Phys. Rev. Lett.* **2016**, *117*, 138301. [[CrossRef](#)] [[PubMed](#)]
22. Rocks, J.; Ronellenfitch, H.; Liu, A.J.; Katifori, E. Limits of multifunctionality in tunable networks. *Proc. Natl. Acad. Sci. USA* **2019**, *116*, 2506–2511. [[CrossRef](#)] [[PubMed](#)]
23. Sangiorgi, S.; De Benedictis, A.; Protasoni, M.; Manelli, A.; Reguzzoni, M.; Cividini, A.; Dell’Orbo, C.; Tomei, G.; Balbi, S. Early-stage microvascular alterations of a new model of controlled cortical traumatic brain injury: 3D morphological analysis using scanning electron microscopy and corrosion casting. *J. Neurosurg.* **2013**, *118*, 763–774. [[CrossRef](#)] [[PubMed](#)]
24. Hartung, G.; Vesel, C.; Morley, R.; Alaraj, A.; Sled, J.; Kleinfeld, D.; Linninger, A. Simulations of blood as a suspension predicts a depth dependent hematocrit in the circulation throughout the cerebral cortex. *PLoS Comput. Biol.* **2018**, *14*, e1006549. [[CrossRef](#)]
25. Schmid, F.; Barrett, M.J.P.; Obrist, D.; Weber, B.; Jenny, P. Red blood cells stabilize flow in brain microvascular networks. *PLoS Comput. Biol.* **2019**, *15*, e1007231. [[CrossRef](#)]
26. Flouraboue, F.; Cloetens, P.; Fonta, C.; Steyer, A.; Lauwers, F.; Marc-Vergnes, J.P. X-ray high-resolution vascular network imaging. *J. Microsc.* **2004**, *215*, 139–148. [[CrossRef](#)]
27. Heinzer, S.; Kuhn, G.; Krucker, T.; Ulmann-Schuler, E.M.A.; Stampanoni, M.; Gassmann, M.; Marti, H.H.; Muller, R.; Vogel, J. Novel three-dimensional analysis tool for vascular trees indicates complete micro-networks, not single capillaries, as the angiogenic endpoint in mice overexpressing human VEGF(165) in the brain. *NeuroImage* **2008**, *39*, 1549–1558. [[CrossRef](#)]
28. Reichold, J.; Stampanoni, M.; Keller, L.; Buck, A.; Jenny, P.; Weber, B. Vascular graph model to simulate the cerebral blood flow in realistic vascular networks. *J. Cereb. Blood Flow Metab.* **2009**, *29*, 1429–1443. [[CrossRef](#)]
29. Waelchli, T.; Bisschop, J.; Miettinen, A.; Ulmann-Schuler, A.; Hintermueller, C.; Meyer, E.P.; Krucker, T.; Waelchli, R.; Monnier, P.P.; Carmeliet, P.; et al. Hierarchical imaging and computational analysis of three-dimensional vascular network architecture in the entire postnatal and adult mouse brain. *Nat. Protoc.* **2021**, *16*, 4564–4610. [[CrossRef](#)]
30. Reichold, J. Cerebral Blood Flow Modeling in Realistic Cortical Microvascular Networks. Ph.D. Thesis, Faculty of Science, ETH Zürich, Zürich, Switzerland, 2011.
31. Demene, C.; Tiran, E.; A.Sieu, L.; Bergel, A.; Gennisson, J.L.; Pernot, M.; De eux, T.; Cohen, I.; Tanter, M. 4D microvascular imaging based on ultrafast Doppler tomography. *NeuroImage* **2016**, *127*, 472–483. [[CrossRef](#)]
32. Hlushchuk, R.; Haberthuer, D.; Soukup, P.; Barré, S.F.; Khoma, O.Z.; Schittny, J.; Jahromi, N.H.; Bouchet, A.; Engelhardt, B.; Djonov, V. Innovative high-resolution microCT imaging of animal brain vasculature. *Brain Struct. Funct.* **2020**, *225*, 2885–2895. [[CrossRef](#)]
33. Ghavanati, S.; Yu, L.X.; Lerch, J.P.; Sled, J.G. A perfusion procedure for imaging of the muse cerebral vasculature by X-ray micro-CT. *J. Neurosci. Methods* **2014**, *221*, 70–77. [[CrossRef](#)]
34. Chung, K.; Wallace, J.; Kim, S.Y.; Kalyanasundaram, S.; Andalman, A.S.; Davidson, T.J.; Mirzabekov, J.J.; Zalocusky, K.A.; Mattis, J.; Denisin, A.K.; et al. Structural and molecular interrogation of intact biological systems. *Nature* **2013**, *497*, 332–337. [[CrossRef](#)]
35. Susaki, E.A.; Tainaka, K.; Perrin, D.; Kishino, F.; Tawara, T.; Watanabe, T.M.; Yokoyama, C.; Onoe, H.; Eguchi, M.; Yamaguchi, S.; et al. Whole-brain imaging with single-cell resolution using chemical cocktails and computational analysis. *Cell* **2014**, *157*, 726–739. [[CrossRef](#)]
36. Dodt, H.U.; Leischner, U.; Schierloh, A.; Jahrling, N.; Mauch, C.P.; Deininger, K.; Deussing, J.M.; Eder, M.; Zieglgansberger, W.; Becker, K. Ultramicroscopy: three-dimensional visualization of neuronal networks in the whole mouse brain. *Nat. Methods* **2007**, *4*, 331–336. [[CrossRef](#)] [[PubMed](#)]
37. Ertuerk, A.; Becker, K.; Jaehrling, N.; Mauch, C.P.; Hojer, C.D.; Egen, G.J.; Hellal, F.; Bradke, F.; Sheng, M.; Dodt, H.U. Three-dimensional imaging of solvent-cleared organs using 3DISCO. *Nat. Protoc.* **2012**, *7*, 1983–1995. [[CrossRef](#)]
38. Hama, H.; Kurokawa, H.; Kawano, H.; Ando, R.; Shimogori, T.; Noda, H.; Fukami, K.; Sakaue-Sawano, A.; Miyawaki, A. Scale: a chemical approach for fluorescence imaging and reconstruction of transparent mouse brain. *Nat. Neurosci.* **2011**, *14*, 1481–1488. [[CrossRef](#)]
39. Ke, M.T.; Fujimoto, S.; Imai, T. SeeDB: a simple and morphology-preserving optical clearing agent for neuronal circuit reconstruction. *Nat. Neurosci.* **2013**, *16*, 1154–1161. [[CrossRef](#)]
40. Renier, N.; Wu, Z.; Simon, D.J.; Yang, J.; Ariel, P.; Tessier-Lavigne, M. iDISCO: a simple, rapid method to immunolabel large tissue samples for volume imaging. *Cell* **2014**, *159*, 896–910. [[CrossRef](#)]
41. Li, Y.; Xu, J.; Wan, P.; Yu, T.; Zhu, D. Optimization of GFP fluorescence preservation by a modified uDISCO clearing protocol. *Front. Neuroanat.* **2021**, *12*, 67. [[CrossRef](#)] [[PubMed](#)]
42. Chung, K.; Deisseroth, K. CLARITY for mapping the nervous system. *Nat. Methods* **2013**, *10*, 508–513. [[CrossRef](#)] [[PubMed](#)]
43. Tomer, R.; Ye, L.; Hsueh, B.; Deisseroth, K. Advanced CLARITY for rapid and high-resolution imaging of intact tissues. *Nat. Protoc.* **2014**, *9*, 1682–1697. [[CrossRef](#)]
44. D.Spence, R.; Kurtha, F.; Itoh, N.; Mongerson, C.R.L.; Wailes, S.H.; Peng, M.S.; MacKenzie-Graham, A.J. Bringing CLARITY to gray matter atrophy. *NeuroImage* **2014**, *101*, 625–632. [[CrossRef](#)]
45. Zheng, H.; Rinaman, L. Simplified CLARITY for visualizing immunofluorescence labeling in the developing rat brain. *Brain Structure and Function* **2016**, *2375–2383*, 221. [[CrossRef](#)]

46. Poplawsky, A.J.; Fukuda, M.; Bok-man Kang, J.; Hwan-Kim, J.; Suh, M.; S. G. Kim. Dominance of layer-specific microvessel dilation in contrast-enhanced high-resolution fMRI: Comparison between hemodynamic spread and vascular architecture with CLARITY. *NeuroImage* **2019**, *197*, 657–667. [[CrossRef](#)]
47. Martínez-Lorenzana, G.; Gamal-Eltrabily, M.; Tello-García, I.A.; Martínez-Torres, A.; Becerra-González, M.; González-Hernández, A.; Condés-Lara, M. CLARITY with neuronal tracing and immunofluorescence to study the somatosensory system in rats. *J. Neurosci. Methods* **2020**, *350*, 109048. [[CrossRef](#)]
48. Ren, Z.; Wu, Y.; Wang, Z.; Hu, Y.; Lu, J.; Liu, J.; Chen, Y.; Yao, M. CUBIC-plus: An optimized method for rapid tissue clearing and decolorization. *Biochem. Biophys. Res. Commun.* **2021**, *568*, 116–123. [[CrossRef](#)]
49. Tainaka, K.; Kubota, S.I.; Suyama, T.Q.; Susaki, E.A.; Perrin, D.; Ukai-Tadenuma, M.; Ukai, H.; Ueda, H.R. Whole-body imaging with single-cell resolution by tissue decolorization. *Cell* **2014**, *159*, 911–924. [[CrossRef](#)]
50. Susaki, E.A.; Tainaka, K.; Perrin, D.; Yukinaga, H.; Kuno, A.; Ueda, H.R. Advanced CUBIC protocols for whole-brain and whole-body clearing and imaging. *Nat. Protoc.* **2015**, *10*, 1709–1727. [[CrossRef](#)]
51. Pinheiro, T.; Mayor, I.; Edwards, S.; Joven, A.; Kantzer, C.G.; Kirkham, M.; Simon, A. CUBIC-f: An optimized clearing method for cell tracing and evaluation of neurite density in the salamander brain. *J. Neurosci. Methods* **2021**, *348*, 109002. [[CrossRef](#)]
52. Hasegawa, S.; Susaki, E.A.; Tanaka, T.; Komaba, H.; Wada, T.; Fukagawa, M.; R.Ueda, H.; Nangaku, M. Comprehensive three-dimensional analysis (CUBIC-kidney) visualizes abnormal renal sympathetic nerves after ischemia/reperfusion injury. *Kidney Int.* **2019**, *96*, 129–138. [[CrossRef](#)]
53. Murakami, T.C.; Mano, T.; Saikawa, S.; Horiguchi, S.A.; Shigeta, D.; Baba, K.; Sekiya, H.; Shimizu, Y.; Tanaka, K.F.; Kiyonari, H.; et al. A three-dimensional single-cell-resolution whole-brain atlas using CUBIC-X expansion microscopy and tissue clearing. *Nat. Neurosci.* **2018**, *21*, 625–637. [[CrossRef](#)] [[PubMed](#)]
54. Matsumoto, K.; Mitani, T.T.; Horiguchi, S.A.; Kaneshiro, J.; Murakami, T.C.; Mano, T.; Fujishima, H.; Konno, A.; Watanabe, T.M.; Hirai, H.; et al. Advanced CUBIC tissue clearing for whole-organ cell profiling. *Nature Protocols* **2021**, *14*, 3506–3537. [[CrossRef](#)] [[PubMed](#)]
55. Karc, R.; Neumann, F.; Neumann, M.; Schreiner, W. Staged growth of optimized arterial model trees. *Ann. Biomed. Eng.* **2000**, *28*, 495–511. [[CrossRef](#)] [[PubMed](#)]
56. Karch, R.; Neumann, F.; Podesser, B.K.; Neumann, M.; Szawlowski, P.; Schreiner, W. Fractal properties of perfusion heterogeneity in optimized arterial trees: a model study. *J. Gen. Physiol.* **2003**, *122*, 307–322. [[CrossRef](#)]
57. Schreiner, W.; Karch, R.; Neumann, M.; Neumann, F.; Roedler, S.M.; Heinze, G. Heterogeneous perfusion is a consequence of uniform shear stress in optimized arterial tree models. *J. Theor. Biol.* **2003**, *3*, 285–301. [[CrossRef](#)]
58. Sakadzic, S.; Roussakis, E.; Yaseen, M.A.; Mandeville, E.T.; Srinivasan, V.J.; Arai, K.; Ruvinskaya, S.; Devor, A.; Lo, E.H.; Vinogradov, S.A.; et al. Two-photon high-resolution measurement of partial pressure of oxygen in cerebral vasculature and tissue. *Nat. Methods* **2010**, *7*, 755–759. [[CrossRef](#)]
59. Blinder, P.; Shih, A.Y.; Rafie, C.; Kleinfeld, D. Topological basis for the robust distribution of blood to rodent neocortex. *Proc. Natl. Acad. Sci. USA* **2010**, *107*, 12670–12675. [[CrossRef](#)]
60. Keller, A.L.; Schuz, A.; Logothetis, N.K.; Weber, B. Vascularization of cytochrome oxidase-rich blobs in the primary visual cortex of squirrel and macaque monkeys. *J. Neurosci.* **2011**, *31*, 1246–1253. [[CrossRef](#)]
61. Kasischke, K.A.; Lambert, E.M.; Panepento, B.; Sun, A.; Gelbard, H.A.; Burgess, R.W.; Foster, T.H.; Nedergaard, M. Two-photon NADH imaging exposes boundaries of oxygen diffusion in cortical vascular supply regions. *J. Cereb. Blood Flow Metab.* **2011**, *31*, 68–81. [[CrossRef](#)]
62. Sherwin, S.J.; Franke, V.; Peiró, J.; Parker, K. One-dimensional modelling of a vascular network in space-time variables. *J. Eng. Math.* **2003**, *47*, 217–250. [[CrossRef](#)]
63. Boas, D.A.; Jones, S.R.; Devor, A.; Huppert, T.J.; Dale, A.M. A vascular anatomical network model of the spatio-temporal response to brain activation. *NeuroImage* **2008**, *40*, 1116–1129. [[CrossRef](#)] [[PubMed](#)]
64. Lorthois, S.; Cassot, F. Fractal analysis of vascular networks: insights from morphogenesis. *J. Theor. Biol.* **2010**, *262*, 614–633. [[CrossRef](#)] [[PubMed](#)]
65. Peyrounette, M.; Davit, Y.; Quintard, M.; Lorthois, S. Multiscale modelling of blood flow in cerebral microcirculation: details at capillary scale control accuracy at the level of the cortex. *PLoS ONE* **2018**, *13*, e0189474. [[CrossRef](#)] [[PubMed](#)]
66. Linninger, A.A.; Gould, I.G.; Marinnan, T.; Hsu, C.Y.; Chojecki, M.; Alaraj, A. Cerebral Microcirculation and Oxygen Tension in the Human Secondary Cortex. *Ann. Biomed. Eng.* **2013**, *41*, 2264–2284. [[CrossRef](#)] [[PubMed](#)]
67. Hsu, C.Y.; Schneller, B.; Alaraj, A.; Flannery, M.; Zhou, X.J.; Linninger, A. Automatic recognition of subject-specific cerebrovascular trees. *Magn. Reson. Med.* **2016**, *77*, 398–410. [[CrossRef](#)]
68. Hsu, C.Y.; Ghaffari, M.; Alaraj, A.; Flannery, M.; Zhou, X.J.; Linninger, A. Gap-free segmentation of vascular networks with automatic image processing pipeline. *Comput. Biol. Med.* **2017**, *82*, 29–39. [[CrossRef](#)]
69. Buades, A.; Coll, B.; Morel, J.M. A Non-Local Algorithm for Image Denoising. *IEEE Comput. Soc. Conf. Comput. Vis. Pattern Recognit.* **2005**, *2*, 60–65.
70. Hasinoff, S.W. Photon, Poisson Noise. In *Computer Vision*; Ikeuchi K., Ed.; Springer: Boston, MA, USA, 2014.
71. Zana, F.; Klein, J.C. Segmentation of vessel-like patterns using mathematical morphology and curvature evaluation. *IEEE Trans. Image Process.* **2001**, *10*, 1010–1019.
72. Bradley, D.; Roth, G. Adapting Thresholding Using the Integral Image. *J. Graph. Tools* **2007**, *12*, 13–21. [[CrossRef](#)]

73. Soille, P. *Morphological Image Analysis: Principles and Applications*; Springer: Berlin/Heidelberg, Germany, 1999.
74. Lee, T.C.; Kashyap, R.L.; Chu, C.N. Building skeleton models via 3-D medial surface/axis thinning algorithms. *Comput. Vis. Graph. Image Process.* **1994**, *56*, 462–478. [[CrossRef](#)]
75. Kerschnitzki, M.; Kollmannsberger, P.; Burghammer, M.; Duda, G.N.; Weinkamer, R.; Wagermaier, W.; Fratzl, P. Architecture of the osteocyte network correlates with bone material quality. *J. Bone Miner. Res.* **2013**, *28*, 1837–1845. [[CrossRef](#)]
76. Pries, A.R.; Secomb, T.W. *Blood Flow in Microvascular Networks. In Microcirculation*; Elsevier: Amsterdam, The Netherlands, 2008; pp. 3–36.
77. Schmid, F. Cerebral Blood Flow Modeling with Discrete Red Blood Cell Tracking Analyzing Microvascular Networks and Their Perfusion. Ph.D. Thesis, Faculty of Science. ETH Zurich, Zürich, Switzerland, 2017.
78. Pries, A.R.; Secomb, T.W.; Gebner, T.; Sperandio, M.B.; Gross, J.F.; Gaetgens, P. Resistance to Blood Flow in Microvessels In Vivo. *Circ. Res.* **1994**, *75*, 904–915. [[CrossRef](#)]
79. Shapiro, H.M.; Stromberg, D.D.; Lee, D.R.; Wiederhielm, C.A. Dynamic pressures in the pill arterial microcirculation. *Am. J. Physiol.-Leg. Content* **1971**, *221*, 279–283. [[CrossRef](#)]
80. Bullit, E.; Gerig, G.; Pizer, S.M.; Lin, W.; Aylward, S.R. Measuring tortuosity of the intracerebral vasculature from MRA images. *IEEE Trans. Med. Imaging* **2003**, *22*, 1163–1171. [[CrossRef](#)]
81. Su, S.W.; Catherall, M.; Payne, S. The influence of network structure on the transport of blood in the human cerebral microvasculature. *Microcirculation* **2012**, *19*, 175–187. [[CrossRef](#)]
82. Lee, R.M. Morphology of cerebral arteries. *Pharmacol. Ther.* **1995**, *66*, 149–173. [[CrossRef](#)]
83. Olufsen, M.S. A structured tree outflow condition for blood flow in larger systemic arteries. *Am. J. Physiol.* **1999**, *276*, H257–H268. [[CrossRef](#)]
84. Olufsen, M.S.; Peskins, C.S.; Kim, W.Y.; Pedersen, E.M.; Nadim, A.; Larsen, J. Numerical simulation and experimental validation of blood flow in arteries with structured tree outflow conditions. *Ann. Biomed. Eng.* **2000**, *28*, 1281–1299. [[CrossRef](#)]
85. Malvè, M.; Chandra, S.; García, A.; Mena, A.; Martínez, M.A.; Finol, E.A.; Doblaré, M. Impedance-based outflow boundary conditions for human carotid haemodynamics. *Comput. Methods Biomech. Biomed. Eng.* **2014**, *17*, 1248–1260. [[CrossRef](#)]
86. El-Bouri, W.K.; Payne, S.J. Multi-scale homogenization of blood ow in 3-dimensional human cerebral microvascular networks. *J. Theor. Biol.* **2015**, *380*, 40–47. [[CrossRef](#)] [[PubMed](#)]
87. Bui, A.V.; Manasseh, R.; K. Liffman, I.D.Šutalo. Development of optimized vascular fractal tree models using level set distance function. *Med. Eng. Phys.* **2010**, *32*, 790–794. [[CrossRef](#)] [[PubMed](#)]